
Article:
Korsós, M.B. orcid.org/0000-0002-0049-4798, Kontogiannis, I. orcid.org/0000-0002-3694-4527, Shukhobodskaia, D. orcid.org/0000-0001-5302-6253 et al. (3 more authors) (2025) Tracing magnetic signatures through the solar atmosphere in seven eruptive active regions. The Astrophysical Journal, 990 (2). p. 121. ISSN: 0004-637X

https://doi.org/10.3847/1538-4357/adf2a7

The Astrophysical Journal, 990:121 (11pp), 2025 September 10 https://doi.org/10.3847/1538-4357/adf2a7

Tracing Magnetic Signatures through the Solar Atmosphere in Seven Eruptive Active Regions

Marianna B. Korsós[1,2,3], Ioannis Kontogiannis[4,5], Daria Shukhobodskaia[6], Luciano Rodriguez[6], Fabiana Ferrente[7], and Francesca Zuccarello[7]

[1] University of Sheffield, School of Electrical and Electronic Engineering, Amy Johnson Building, Portabello Street, Sheffield, S1 3JD, UK; komabi@gmail.com
[2] Department of Astronomy, Eötvös Loránd University, Pázmány Péter sétány 1/A, H-1112 Budapest, Hungary
[3] Gyula Bay Zoltán Solar Observatory (GSO), Hungarian Solar Physics Foundation (HSPF), Petőfi tér 3, H-5700 Gyula, Hungary
[4] ETH Zürich, Institute for Particle Physics and Astrophysics, Wolfgang-Pauli-Strasse 27, 8093, Zürich, Switzerland
[5] Istituto Ricerche Solari Aldo e Cele Daccó (IRSOL) Locarno, Switzerland
[6] Solar-Terrestrial Centre of Excellence—SIDC, Royal Observatory of Belgium; Avenue Circulaire 3, 1180 Brussels, Belgium
[7] INAF—Catania Astrophysical Observatory, Via S. Sofia 78, I95123 Catania, Italy
Received 2025 April 5; revised 2025 July 17; accepted 2025 July 20; published 2025 September 3

Abstract

This case study focuses on the pre-eruptive conditions of active regions that produced either low-energy flares accompanied by major CMEs (AR 12371 and AR 11692) or major X-class flares also associated with significant CMEs (AR 12673, AR 12158, AR 11520, AR 11429, and AR 13664). The study examines the evolution of 10 morphological parameters that serve as indicators of pre-eruptive conditions—not only at the photosphere but also in higher layers of the solar atmosphere. We found that active regions with a greater number of parameters exceeding their threshold values at higher altitudes tend to exhibit a higher eruptive potential. Specifically, in active regions associated with X-class flares and fast CMEs, at least 8 out of 10 parameters exceeded their thresholds at elevated layers, whereas in the 2 active regions linked to M-class flares and fast CMEs, fewer than 7 parameters did so. These results suggest that assessing the height-dependent behavior of pre-eruptive proxy parameters could significantly improve the identification and prediction of eruptive active regions. Future studies should extend this approach to a larger data set to better determine the maximum atmospheric height at which the predictive thresholds of different parameters are met, thereby enhancing the accuracy of solar eruption prediction.

Unified Astronomy Thesaurus concepts: Solar flares (1496)

1. Introduction

Two of the primary phenomena driving space weather are coronal mass ejections (CMEs; P. F. Chen 2011; D. F. Webb & T. A. Howard 2012) and solar flares (L. Fletcher et al. 2011; K. Shibata & T. Magara 2011). CMEs, massive eruptions of plasma and magnetic fields from the solar corona, can trigger geomagnetic storms that disrupt Earth's magnetosphere, radiation belts, and ionosphere (N. Gopalswamy 2016; A. Patari & A. Guha 2023). These storms may harm satellites, navigation systems, GPS accuracy, and power grids (G. S. Lakhina & B. T. Tsurutani 2016). Solar flares, sudden bursts of radiation, cause immediate ionospheric disturbances (J. J. Curto 2020; A. Buzás et al. 2023), affecting communication systems. Both events accelerate solar energetic particles, further influencing space weather (N. Buzulukova & B. Tsurutani 2022). Predicting the timing and intensity of CMEs and flares remains a significant challenge, despite ongoing research using magnetic field analysis of their primary source regions—magnetically complex active regions (S. Hazra et al. 2020)—and other methods (M. K. Georgoulis et al. 2024).

Studying active regions individually and parameterizing their evolution provides essential data for understanding solar activity and its impacts on the heliosphere (I. Kontogiannis et al. 2018; M. K. Georgoulis et al. 2024). Each parameter offers unique insights into the physical state and energetic potential of active regions, helping to unravel the mechanisms behind solar flares and CMEs. Detailed analysis of active region evolution before large solar eruptions allows us to identify critical precursors of significant solar events, contributing to improved eruption prediction. The relationship between eruption productivity and active region properties has been studied extensively by many researchers. Some have focused on characterizing magnetic field topology, such as shear angles (M. J. Hagyard et al. 1984; Y. Lu et al. 1993) and polarity inversion lines (A. Bruzek 1964; A. Asai et al. 2004), while others have emphasized energetic aspects, like non-neutralized electric current (I. Kontogiannis & M. K. Georgoulis 2024), free magnetic energy, and magnetic helicity (Y. J. Moon et al. 2002; K. D. Leka & G. Barnes 2003; J. Jing et al. 2012; E. Liokati et al. 2022). By combining different parameters, a more comprehensive understanding of the dynamic processes governing AR evolution can be achieved (I. Kontogiannis 2023; R. Miteva et al. 2024), enabling the development of robust predictive models for solar eruptions and their heliospheric consequences.

The magnetic structures in the chromosphere and corona often differ from those seen in the photosphere, as can also be seen in Figure 1, where the complex magnetic structures of AR 13664/8 change throughout the solar atmosphere. This highlights the importance of examining higher atmospheric layers, where evolving magnetic patterns may reveal trends and variability associated with eruptive behavior. Recently, M. B. Korsós et al. (2018) demonstrated that the prediction of major solar eruptions, such as flares, can be enhanced by incorporating data from the lower solar atmosphere, spanning from the photosphere up to approximately 4 Mm above the

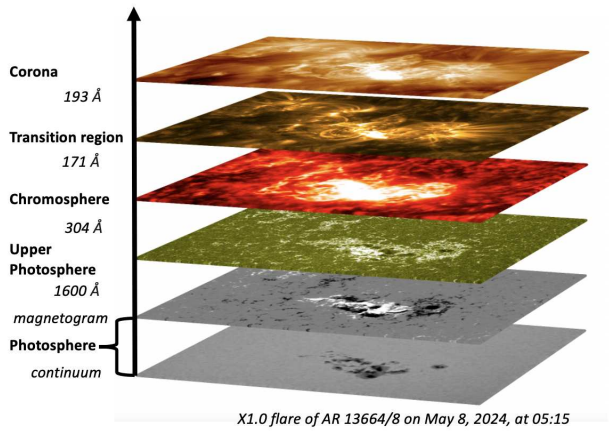

Figure 1. Multilayered visualization of the solar atmosphere during an X1.0 flare from AR 13664/8, observed on 2024 May 8, at 05:15. This composite shows images from various altitudes in the Sun's atmosphere, arranged from bottom to top: the photosphere visible in continuum light, magnetogram highlighting magnetic field structures, upper photosphere at 1600 Å, chromosphere at 304 Å, transition region at 171 Å, and the corona at 193 Å. Each layer captures different plasma temperatures and magnetic conditions associated with the flare, providing a comprehensive view of the dynamic processes across different layers of the Sun's atmosphere.

solar surface. M. B. Korsós et al. (2020) and M. B. Korsós et al. (2022) highlighted that using extrapolation data enables earlier identification of the pre-flare evolution phase of predictor parameters, in particular in the region above the photosphere within the lower solar atmosphere (up to 2 Mm). M. B. Korsós et al. (2024) demonstrated that the derived morphological and proxy parameters evolve similarly when using potential field (PF), linear force-free field (LFFF), or the more complex nonlinear force-free field (NLFFF) extrapolation methods (T. Wiegelmann & T. Sakurai 2021), as well as the physics-based neural network NLFFF (NF2) extrapolation method developed by R. Jarolim et al. (2023). M. B. Korsós et al. (2024) also suggested that it may be more beneficial to investigate the evolution of multiple parameters in parallel throughout the lower solar atmosphere. The promising application of various prediction parameters across the lower solar atmospheric layers was further investigated and confirmed by S. Biswal et al. (2024), S. H. Garland et al. (2024), P. H. Lin et al. (2020), and P. Pagano et al. (2019).

Last year, NOAA AR 13664/8 exhibited intense activity, culminating in the strongest geomagnetic storm since 2003 November, which reached a peak Dst index of −412 nT on 2024 May 11, around 04:00 UTC, as detailed in an overview by H. Hayakawa et al. (2025), N. M. Kondrashova et al. (2024). Due to its significant impact on space weather, from 2024 May 2 to 14, NOAA AR 13664/8 has been extensively studied from various perspectives to understand the evolution of its magnetic complexity (P. Jaswal et al. 2024; D. MacTaggart et al. 2024), the storage of energy within the active region (R. Jarolim et al. 2024; P. Romano et al. 2024), strong magnetic field gradients along the polarity inversion line (R. Wang et al. 2024), and the development of strong electric currents (I. Kontogiannis 2024; Y. Li et al. 2024) during its major flaring events.

Based on the above description, the primary objective of this study is to parameterize the magnetic field evolution of seven selected active regions, including NOAA AR 13664/8. Each region produced flares of varying energy levels (M- or X-class), but all were associated with significant CME eruptions. The pre-eruptive analysis of these active regions from various perspectives is important, e.g., for studies investigating the complete chain of space weather effects, from the Sun to the Earth, as their eruptions triggered geomagnetic storms. Motivated by this, we chose 10 parameters to trace magnetic signatures through the solar atmosphere of these regions, following the methodology outlined in M. B. Korsós et al. (2024). This study aims to assess the height-dependent pre-eruptive behavior of proxy parameters, which could significantly enhance the identification and prediction of major solar eruptions.

This work is structured as follows: Section 2 provides a comprehensive review of the studied solar active regions. In Section 3, we describe the data sets and methodologies employed in this study, focusing on the three-dimensional (3D) analysis techniques used to evaluate the magnetic field structures within the active regions. Section 4 delves into the detailed analysis of the 3D magnetic field evolution of the active regions via different proxy parameters. The conclusion summarizes our key findings and suggests directions for future research based on the insights gained from this study.

2. Overview of Selected Seven Solar Active Regions and Associated Events

In this study, we analyze the evolution of seven active regions through the lower solar atmosphere, using 10 magnetic field parameters provided by the FLARECAST project (M. K. Georgoulis et al. 2021). For more details about these parameters, see Section 4. Among these regions, five produced the X-class flares, while the other two primarily generated M-class flares accompanied by significant CME occurrences. Let us explore these seven active regions in greater detail, as follows:

1. AR 13664/8[8] displayed significant solar activity as it moved across the solar disk from its initial observation on the eastern limb on May 1. By May 5, the region showed moderate magnetic flux, with major polarities rapidly separating and minor ones merging, in particular on the western side of the active region. Simultaneously, AR 13668 emerged on the eastern side of AR 13664 with a simple bipolar layout. As AR 13664's complexity grew, it was classified as a β-δ configuration, escalating the potential for significant flare activity. This complexity evolved into a β-γ-δ structure by May 6, due to the flux enhancements from emerging bipoles in AR 13668, aligning north–south between the older AR 13664 and newer sunspots, increasing regional intricacy. From this point, the region was referred to as AR 13664/8. This increased complexity led to intense flare activity from May 7, peaking with frequent M-class flares and the first X-class flare, an X1.0, on May 8 (see the moment of the first X-class flare in Figure 1) from the fully developed AR 13664/8. This intense activity persisted until May 14, culminating in a series of 12 X-class flares, the most intense being an X8.7 flare on May 14. Our analysis of that active region covers the evolution from May 5 to 12, referring to the entire complex as AR 13664.

[8] http://helio.mssl.ucl.ac.uk/helio-vo/solar_activity/arstats/arstats_page5.php?region=13664

Table 1
Studied Active Regions That Hosted Solar Eruptions Associated with Geomagnetic Storms

NOAA-HARP	Magn. Class	Flare Peak (UTC)	GOES Class	CME Time (UTC)	Speed (km s^{-1})
13664/8-11149	β-γ-δ	8-May-2024 05:09 / 21:40	X1.0 / X1.1	8-May-2024 05:36 / 22:24	920 ± 185 / 1150 ± 230
⋯	⋯	9-May-2024 09:13 / 17:44	X2.2 / X1.1	9-May-2024 09:24 / 18:52	1540 ± 310 / 980 ±200
⋯	⋯	10-May-2024 06:27	X3.9	10-May-2024 07:12	910 ± 180
⋯	⋯	11-May-2024 01:23 / 11:44	X5.8 / X1.5	11-May-2024 01:36	1340 ± 270
11429-1449	β-γ-δ	7-Mar-2012 00:24 / 01:05	X5.4 / X1.3	7-Mar-2012 00:24	2100 ± 420
11520-1834	β-γ-δ	12-Jul-2012 16:49	X1.4	12-Jul-2012 16:48	1210 ± 240
12158-4536	β-γ-δ	10-Sep-2014 17:45	X1.6	10-Sep-2014 18:00	1410 ± 280
12673-7115	β-γ-δ	6-Sep-2017 12:02	X9.3	6-Sep-2017 12:24	1670 ± 330
11692-2546	β	15-Mar-2013 06:58	M1.1	15-Mar-2013 07:12	1260 ± 250
12371-5692	β-γ-δ	21-Jun-2015 02:36	M2.6	21-Jun-2015 02:36	1580 ± 320

Note. Columns list the NOAA and HARP region numbers, magnetic classification at the time of eruption, flare timing and class (GOES), CME launch time from SOHO LASCO-C2, and CME speed from the GCS model (A. Thernisien 2011).

2. AR 11429[9] was analyzed from 2012 March 5 to 15. This active region was already in its developed phase when it rotated into view from the far side of the Sun and was characterized by a β-γ-δ magnetic configuration, which exhibited significant activity. It produced an X5.4-flare on 2012 March 7, at 00:24, followed by another X1.3 flare shortly thereafter, highlighting the complexity of its magnetic interactions. These flares, which were associated with very fast CMEs (2100 km s^{-1}), triggered geomagnetic storms on Earth, in particular those noted on 2012 March 8.
3. Similar to the previous active region, AR 11520[10] was also in a developed phase and characterized by a β-γ-δ magnetic class. We analyze the evolution of the active region from 2012 July 10. AR 11520 was a pivotal source of solar disturbances in 2012 July. On 2012 July 12, it produced an X1.4-flare at 16:49, immediately followed by a CME with a speed of 1210 km s^{-1} that impacted Earth on 2012 July 15.
4. Similar to AR 11429 and AR 11520, AR 12158[11] was also in a developed phase when it turned to the front side of the Sun. We observed the evolution of AR 12158 from 2014 September 6. Holding a β-γ-δ configuration, AR 12158 was responsible for an X1.6 flare on 2014 September 10. The subsequent CME was recorded with speed at about 1410 km s^{-1}, contributing to geomagnetic disturbances observed on Earth on 2014 September 12.
5. AR 12673[12] demonstrated significant solar activity. Our detailed analysis of the evolution of the active region began on 2017 September 2, as the region started to show developmental patterns similar to those of AR 13664/8. The most notable event occurred when the active region was already in a β-γ-δ magnetic configuration, on 2017 September 6, at 12:02, leading to an intense X9.3-flare recorded at 12:24. This flare was followed by a fast CME, which reached speeds up to 1670 km s^{-1}. The CME reached Earth on 2017 September 7.
6. AR 11692[13] had a simpler β magnetic configuration but still caused significant geomagnetic effects during its disk passage from 2013 March 11–20. It produced an M1.1 flare on 2013 March 15, with a subsequent CME traveling at about 1260 km s^{-1}, leading to notable geomagnetic activity on Earth by 2013 March 17.
7. Observed from 2015 June 17 to 27, AR 12371[14] exhibited a β-γ-δ class and generated a 1580 km s^{-1} CME associated with an M2.6 flare on 2015 June 21. This event led to geomagnetic effects noted on Earth the following day, reflecting the region's potential for inducing substantial space weather activities.

The details of the active regions are summarized in Table 1. The corresponding CME speeds were estimated using the graduated cylindrical shell (GCS) model (A. Thernisien 2011), which enables three-dimensional reconstruction of the CME front from simultaneous multi-viewpoint coronagraph observations. The use of both LASCO and STEREO-A data reduces projection effects and improves the accuracy of the results compared to plane-of-sky speeds listed in the LASCO CME catalog. Based on the sensitivity analysis of A. Thernisien et al. (2009), typical uncertainties when using two viewpoints are approximately $\sim 4.^{\circ}3$ in longitude and $\pm 1.^{\circ}8$ in latitude, with maximum deviations of up to $16.^{\circ}6$ and $3.^{\circ}7$, respectively. These values are consistent with more recent findings by C. Verbeke et al. (2023), who showed that dual-viewpoint reconstructions significantly reduce uncertainties compared to single-spacecraft fits, and with C. Kay & E. Palmerio (2024), who reported average differences of $\sim 4°$ in latitude, $\sim 8°$ in longitude, and $\sim 19\%$ in radial velocity between independent GCS reconstructions of the same CME. Based on

[9] http://helio.mssl.ucl.ac.uk/helio-vo/solar_activity/arstats/arstats_page5.php?region=11429
[10] http://helio.mssl.ucl.ac.uk/helio-vo/solar_activity/arstats/arstats_page5.php?region=11520
[11] http://helio.mssl.ucl.ac.uk/helio-vo/solar_activity/arstats/arstats_page5.php?region=12158
[12] http://helio.mssl.ucl.ac.uk/helio-vo/solar_activity/arstats/arstats_page5.php?region=12673
[13] http://helio.mssl.ucl.ac.uk/helio-vo/solar_activity/arstats/arstats_page5.php?region=11692
[14] http://helio.mssl.ucl.ac.uk/helio-vo/solar_activity/arstats/arstats_page5.php?region=12371

these results, we adopt a conservative uncertainty of 20% in the radial speed.

3. The Data and Applied Method for the 3D Analyses

Researchers have introduced novel magnetic properties that capture various facets of energy storage mechanisms in active regions. Significant progress in this research was spurred by the launch of the Solar Dynamics Observatory (SDO; W. D. Pesnell et al. 2012), which provided a continuous stream of high-quality, near-real-time photospheric vector magnetograms of active regions through the HMI-Helioseismic and Magnetic Imager (P. H. Scherrer et al. 2012). To further support both research and operational needs, the HMI team introduced Space Weather HMI Active Region Patches (SHARPs), which are cutouts of vector magnetograms of regions of interest (such as active regions), accompanied by a set of predictors suitable for space weather research (M. G. Bobra et al. 2014). This type of data enabled the study of active region evolution leading up to significant solar eruptions by analyzing the changes in prediction parameters at the photospheric level.

However, the field of solar eruption prediction still faces significant challenges, some of which can be addressed by studying the evolution of morphological parameters in the lower solar atmosphere (M. B. Korsós et al. 2018). To determine the 3D magnetic field structures of the seven studied active regions, we utilized the linear force-free field (LFFF) extrapolation method, as in M. B. Korsós et al. (2024). It is important to bear in mind that the choice of coronal extrapolation model can influence the results. M. B. Korsós et al. (2024) compared the evolution of six prediction parameters (most of which are also used in this work) from the photosphere up to the lower corona in both intensely flaring and more quiescent, yet magnetically complex, active region cases. They used four extrapolation methods: potential field (PF), LFFF, and two types of nonlinear force-free field (NLFFF) models. They found that, although the overall trends in parameter evolution were similar across methods, the parameter magnitudes were generally higher when using NLFFF, leading to threshold crossings at higher atmospheric heights compared to the PF or LFFF results. M. B. Korsós et al. (2024) also concluded that, for quick yet reasonably reliable insights into the 3D pre-flare evolution of active regions, both PF and LFFF extrapolations are acceptable, as they produced very similar patterns—albeit less accurate than those from NLFFF. Based on M. B. Korsós et al. (2024), in the lower atmosphere (below $\sim$1 Mm), the timing discrepancy in threshold crossings between NLFFF and LFFF was typically small, usually less than 10 hr. However, this difference increased with height, and above $\sim$1 Mm, LFFF-derived parameters could reach their thresholds 30%–50% later in time compared to NLFFF. This growing lag aligns with the increasing divergence in magnetic field magnitudes: NLFFF magnetic field values can exceed LFFF estimates by approximately 15%–25% between 1 and 3 Mm. These differences arise from the simplified linear assumptions of LFFF, especially at greater heights. Nevertheless, the overall evolutionary behavior of the parameters remains consistent across methods, and LFFF continues to offer a computationally efficient and practically useful tool for 3D pre-eruptive diagnostics.

With this in mind, the LFFF method is considered suitable for our analysis in this work. The lower boundary of LFFF is the *hmi. sharp_cea_720s* photospheric vector magnetic field measurements at every moment of time, namely the B_r, B_t, and B_p components. We constructed the extrapolated magnetogram data from the $z = 0$ level (representing the photosphere) up to $\sim$7 Mm in the lower solar atmosphere with a 60 minute cadence using the model by T. Wiegelmann et al. (2012). The step size in the vertical direction used is $z = 0.36$ Mm, which matches the SHARP pixel size. Furthermore, for the LFFF extrapolation, the already calculated and stored total twist parameter α in the fits-header of the SHARP data series was used. We selected 10 parameters from the FLARECAST project website[15] and analyzed their temporal evolution through the lower solar atmosphere before the geoeffective solar eruptions. The selection of these 10 parameters was based on their recognition as effective predictors in the literature (see the related references in Section 4) and their inclusion in the FLARECAST project (M. K. Georgoulis et al. 2021).

4. Analysis of the 3D Skeleton of Active Regions

In this section, we discuss the parameters and the characteristic behaviors identified prior to the studied solar eruptions. It is important to note that all threshold values and pre-flare behaviors for these parameters were previously defined based on studies conducted at the photospheric level (see the relevant subsections below for each parameter). While it is well known that magnetic field structures and their evolution vary with atmospheric height, establishing new thresholds at each layer would require extensive statistical analyses at those altitudes. Therefore, the most practical approach is to apply the thresholds established at the photosphere and investigate up to which height they remain valid. We then assess whether the persistence of these conditions at higher layers further supports the eruptive potential of the active region.

4.1. Total Unsigned Magnetic Flux—Φ_{TOT}

First, let us discuss the total unsigned magnetic flux ($\Phi_{\rm TOT}$). The $\Phi_{\rm TOT}$ represents the total amount of magnetic field passing through a surface, regardless of polarity. As we move upward from the photosphere into the solar atmosphere, the magnitude of $\Phi_{\rm TOT}$ typically decreases with height, as the magnetic field strength gradually weakens. Monitoring $\Phi_{\rm TOT}$ allows us to identify regions where magnetic energy is accumulating, which can potentially lead to solar flares. Previous studies have shown that active regions with $\Phi_{\rm TOT}$ exceeding approximately 10^{22} Mx are more likely to produce significant solar flares and/or CMEs (A. Shanmugaraju et al. 2023, and references therein). Furthermore, T. Li et al. (2021), who analyzed 719 GOES-class flares between 2010 and 2019, found that active regions with magnetic flux above 10^{23} Mx have a higher probability of producing M- or X-class flares.

In our analysis of the selected active regions, we adopt the commonly used threshold of 10^{22} Mx. In all examined cases, $\Phi_{\rm TOT}$ exceeded this threshold between the photosphere and 7 Mm. Notably, AR 13664 exhibited the highest values, with approximately 8×10^{22} Mx at the photosphere and around 3×10^{22} Mx at 7 Mm prior to the flare. For the temporal evolution of $\Phi_{\rm TOT}$ in AR 13664, see Figure 2(a). Furthermore, ARs 11429, 11520, 12158, and 12673 exhibited values of approximately 9, 6, 4, and 5×10^{22} Mx at the photosphere, and around 4, 4, 2, and 2×10^{22} Mx at 7 Mm prior to the flare,

[15] https://dev.flarecast.eu/stash/projects/FE

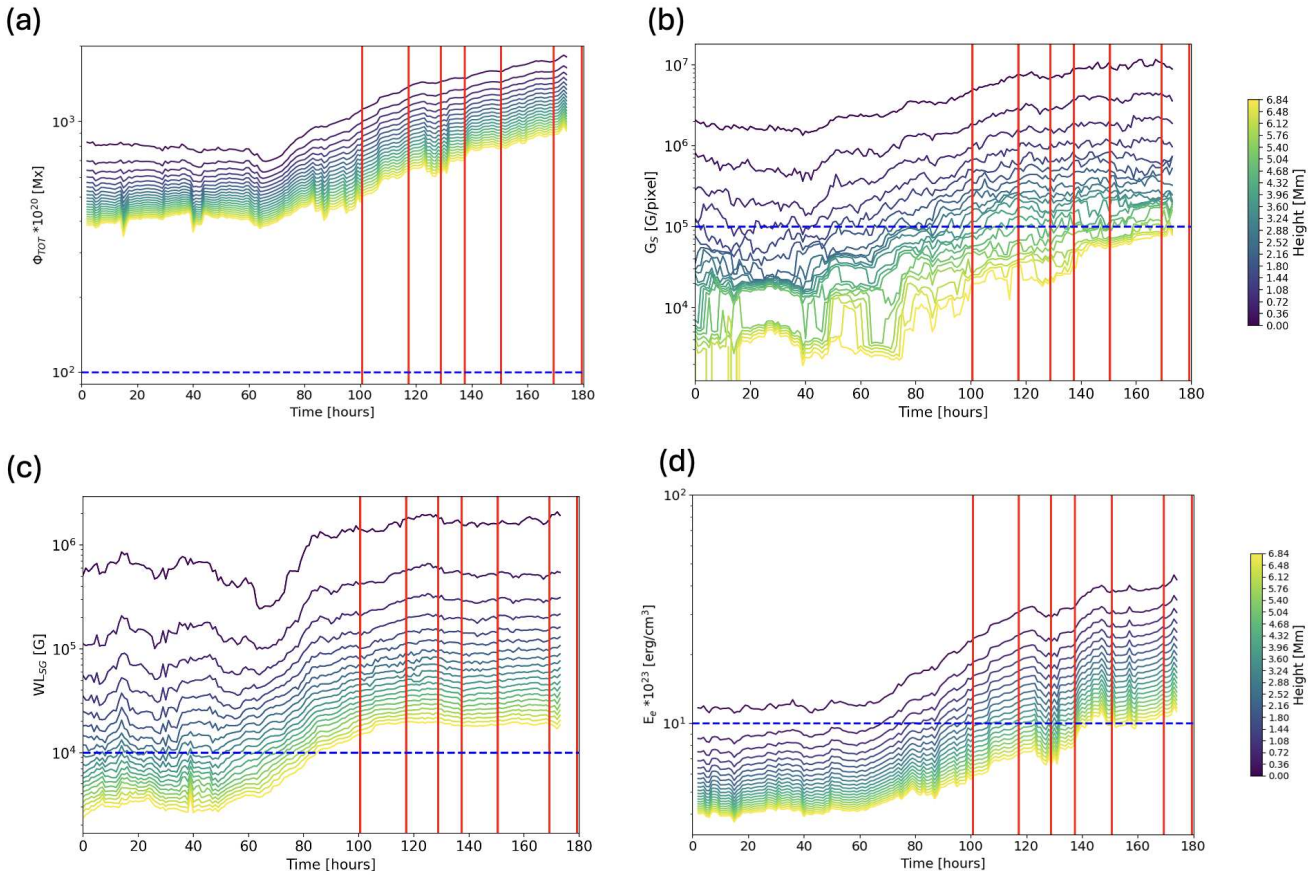

Figure 2. The panels show the evolution of (a) $\Phi_{\rm TOT}$, (b) G_S, (c) $\rm WG_{LS}$, and (d) E_e parameters over time at different atmospheric heights for active region AR 13664. The color bar represents the heights at which the parameters were calculated, expressed as multiples of 0.36 Mm, which corresponds to the grid step size in the z-direction of an SDO pixel size, e.g., $0^{*}0.36$ Mm is the photosphere, $7^{*}0.36$ Mm = 2.5 Mm above the photosphere. The blue horizontal lines represent the corresponding threshold level of the given parameter. Red vertical lines indicate the occurrence of solar flares on specific dates and times: 2024 May 8 at 05:09 (X1.0), 2024 May 8 at 21:08 (X1.0), 2024 May 9 at 09:13 (X2.2), 2024 May 9 at 17:44 (X1.1), 2024 May 10 at 06:54 (X3.9), and 2024 May 11 at 01:23 (X5.8). Data are recorded every 60 minutes starting from 2024 May 4.

respectively. ARs 11692 and 12371, which were associated with lower-energy flares, showed values of about 6 and 7×10^{22} Mx at the photosphere, and approximately 2 and 3×10^{22} Mx at 7 Mm before the flare.

4.2. *Horizontal Magnetic Gradient*—$\rm G_S$

The horizontal magnetic gradient G_S, as introduced by M. B. Korsós & R. Erdélyi (2016), serves as a morphological parameter that quantifies the magnetic interactions within a sunspot group, especially focusing on the horizontal magnetic gradient between opposite polarities. According to I. Kontogiannis et al. (2018), if the horizontal magnetic gradient reaches or exceeds 10^5 G pixel^{-1}, there is an increased likelihood of larger solar flares occurring.

In the case of AR 13664, this parameter exceeded the threshold level—reaching 10×10^5 G pixel^{-1} in the photosphere—four days before the solar eruption. Notably, it remained above 10^5 G pixel^{-1} at approximately 3 Mm even four hours prior to the eruption, as shown in Figure 2(b). In other active regions, the parameter also remained above the threshold at various atmospheric heights for extended periods before the flare, often reaching up to the chromosphere. For example, G_S reached approximately 15, 25, 9, and 10×10^5 G pixel^{-1} at the photosphere in ARs 11429, 11520, 12158, and 12673, respectively, and remained above the threshold up to about 2.4 Mm in AR 11429, 1.8 Mm in AR 11520, 0.7 Mm in AR 12158, and 2.4 Mm in AR 12673. Even in active regions that produced lower-energy flares (i.e., less than X-class), the parameter still exceeded the threshold at lower heights: in AR 11692, with approximately 6×10^5 G pixel^{-1} at the photosphere, it remained above the threshold up to about 0.4 Mm; and in AR 12371, with about 10×10^5 G pixel^{-1} at the photosphere, it remained above the threshold up to around 1 Mm.

4.3. *Gradient-weighted Integral Length of the Neutral Line—WL_{SG}*

The purpose of the gradient-weighted integral length of the neutral line $\rm WL_{SG}$ is to indirectly quantify the free magnetic energy of an active region. This proxy considers the strong-field intervals of the polarity inversion line (PIL) to be those where the horizontal field, computed from the vertical field component of the magnetogram, is >150 G. $\rm WL_{SG}$ has units of Gauss G. The probability of a major solar eruption decreases as $\rm WL_{SG}$ decreases, and it approaches zero when $\rm WL_{SG}$ falls below approximately 10^4 G. D. A. Falconer et al. (2012) concluded that a major solar eruption could be expected with 75% probability in the next 24 hr prediction window if $\rm WL_{SG} > 10^4$ G.

For all the studied active regions, the WL_{SG} parameter was above the threshold level from the photosphere up to certain heights. Specifically, for AR 13664 (see Figure 2(c)), WL_{SG} exceeded the threshold from the photosphere—where it reached approximately 4×10^6 G—up to the chromosphere (around 2 Mm), where it was still about 10^4 G. Furthermore, ARs 11429, 11520, 12158, and 12673 exhibited photospheric magnetic field strengths of approximately 8, 3, 5, and 10×10^5 G, and remained above 10^4 G at heights of 6, 2, 2, and 7 Mm, respectively, prior to the flare. In contrast, ARs 11692 and 12371, which were associated with lower-energy flares, showed field strengths of about 7 and 5×10^5 G at the photosphere, and approximately 10^4 G at heights of 1 and 2 Mm, respectively, before the flare.

4.4. Total Excess Magnetic Energy—E_e

Total excess magnetic energy (E_e; K. D. Leka & G. Barnes 2007) is the sum of the moments of excess magnetic energy density, a parameter introduced by J. Wang et al. (1996) at the photosphere. This parameter incorporates the angular shear between vectors of the observed magnetic field and its corresponding magnetic vector relative to the solar surface. J. Wang et al. (1996) described their definition of the shear angle as directly corresponding to the non-potential field and the magnetic energy stored in the non-potential magnetic field, which they defined as free magnetic energy. Furthermore, J. Wang et al. (1996) showed that the density of free energy can be expressed in terms of angular shear, as well as the magnitude of the observed and potential vector fields. Therefore, the two-dimensional mapping of free energy density correlates with stronger solar events produced by an active region. Subsequently, K. D. Leka & G. Barnes (2007) demonstrated that E_e serves as a reliable parameter for flare prediction, with higher values increasing the likelihood of producing large flares, in particular when it exceeds 10^{24} erg cm^3.

It is noteworthy that E_e reached the threshold level only in the cases of AR 13664, AR 11429, and AR 11520. However, for AR 12158, AR 12673, AR 11692, and AR 12371, it did not. Interestingly, in four of these active regions, E_e was just close to the threshold, with values ranging between 0.7×10^{24} erg cm^{-3} and 0.9×10^{24} erg cm^{-3}. In the case of AR 13664 (see Figure 2(d)), E_e exhibited an increasing trend leading up to the solar eruption, consistent with the region being in an evolutionary phase. From the beginning, E_e was slightly above 10^{24} erg cm^{-3} at the photosphere and only reached the threshold much later at the maximum height of approximately 2 Mm.

The parameter consistently exceeded the threshold over a similar timeframe as at the photosphere, maintaining levels of 1.6×10^{24} and 1.3×10^{24} erg cm^{-3} in AR 11429 and AR 11520, respectively. For these two active regions, E_e remained stable at a height of approximately 0.4 Mm, with values around 1.4×10^{24} and 1.1×10^{24} erg cm^{-3}, respectively, reflecting their more developed phase.

4.5. Main Polarity Inversion Line—MPIL

The polarity inversion line (PIL) separates patches of positive and negative fluxes, where the gradient of the magnetic field is large and indicative of strong shearing or twisting of the magnetic field structure of an active region. The main polarity inversion line (MPIL) separates the major polarity regions of an active region. D. A. Falconer et al. (2003) studied the CME predictability of the measured MPIL, while J. P. Mason & J. T. Hoeksema (2010) found that it could also be used for flare prediction purposes. They suggested that a large solar eruption could be anticipated within a two-day period if the MPIL exceeds the threshold of 62 Mm, where the observed transverse field strength is greater than 150 Gauss. Furthermore, the length of the MPIL correlates strongly with CME speed, as shown by I. Kontogiannis et al. (2019).

In the case of AR 13664, the MPIL exceeded the 62 Mm threshold from the photosphere about 4 days before the first X-class flare and the associated CME, and up to ∼2.5 Mm about 8 hr prior to the flare (see Figure 3(a)). For AR 11429 and AR 11520, the MPIL consistently exceeded the 62 Mm threshold from the photosphere up to heights of ∼7 Mm and ∼1.5 Mm, respectively, for two to three continuous days before the observed flare and CME eruption. In the cases of AR 12158 and AR 12673, the MPIL exceeded the 62 Mm threshold up to heights of approximately 1.2 Mm and 3 Mm, respectively. At the photospheric level, the MPIL reached this threshold 113 hr earlier for AR 12158 and 67 hr earlier for AR 12673. At the maximum heights, the threshold was exceeded 58 hr before the eruption in AR 12158 and 5 hours earlier in AR 12673. Notably, for AR 11692, the MPIL exceeded the 62 Mm threshold only at the photosphere, 87 hr prior to the eruption. In contrast, for AR 12371, the MPIL remained above this threshold up to approximately 2 Mm continuously for about three days before the associated flare and CME eruption. Except for AR 11692, all other active regions exhibited MPIL lengths greater than 100 Mm at the photosphere, with the lengths decreasing as the height increased.

4.6. R-value Parameter

Large flares are consistently linked to regions with strong magnetic gradients, often associated with the emergence of magnetic elements carrying electrical currents through the photosphere. To assess these regions, we used the so-called R-value, which estimates the total unsigned flux within approximately 15 Mm of strong-field areas along high-gradient polarity-separation lines (C. J. Schrijver 2007). As the R-value increases, more magnetic free energy becomes available, potentially fueling larger flares and increasing the likelihood of major solar eruptions. C. J. Schrijver (2007) found that, when $\log R > 5.0$, at least one major flare is expected to occur within 24 hr.

For the active regions studied here, the R-value was above its threshold at the photosphere at least two days before the studied large solar eruptions. An exception was AR 11692, where the R-value remained around 4 just prior to the solar eruption, likely due to the simpler magnetic configuration of this region (classified as a β-type region). Additionally, the parameter slightly exceeded the threshold above the photosphere in other cases: for AR 11429, it was two days before the solar eruption at approximately 0.4 Mm; for AR 13664 (Figure 3(b)) and AR 12673, it was 10 hr and 37 hr before the eruptions, respectively, at a height of 720 km.

4.7. Magnetic Helicity Injection—$\dot{H}$

The studies by B. J. LaBonte et al. (2007) and S.-h. Park et al. (2010) investigated the correlation between the magnetic helicity injection rate in the volume ($\dot{H}$) and the occurrence of X-class solar flares. Results reveal that active regions capable of producing X-class flares invariably exhibit a peak surpassing 4.5×10^{40}–48×10^{40} Mx^2 hr^{-1} for 0.5–2 days. Recently,

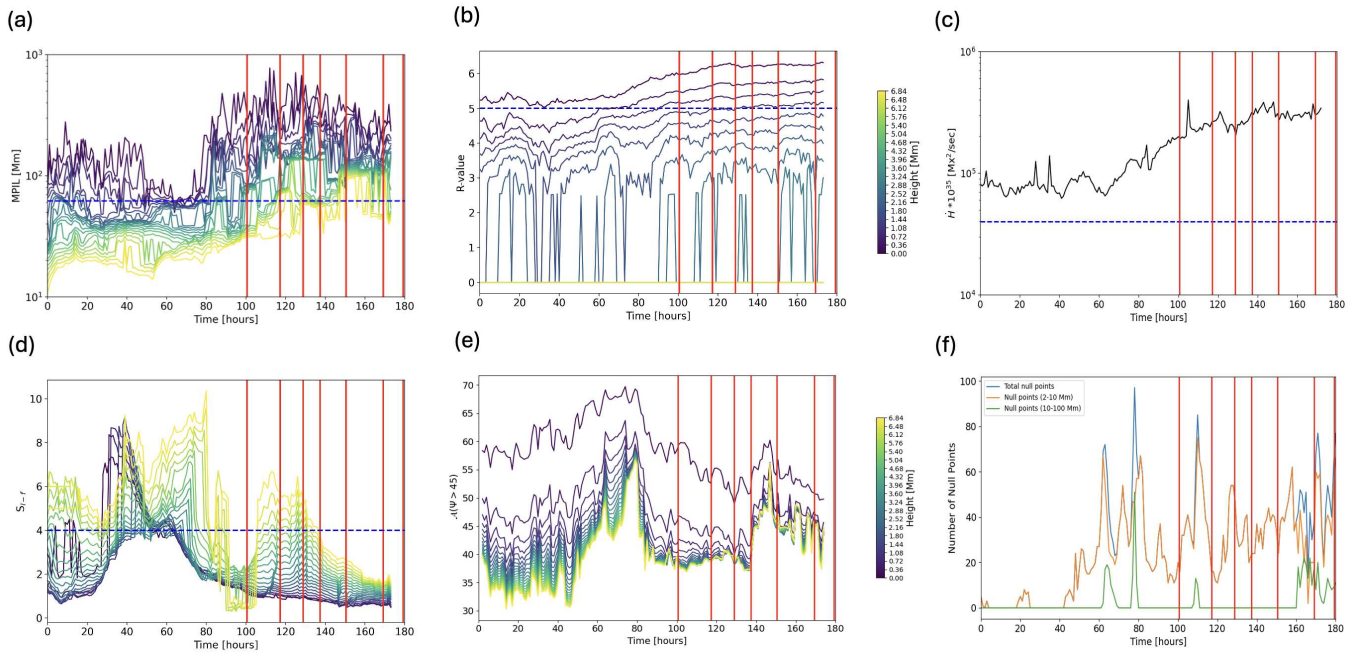

Figure 3. This figure is similar to Figure 2; however, the panels display the evolution of (a) MPIL, (b) R-value, (c) $\dot{H}$, (d) S_{l-f}, (e)$\mathcal{A}(\Psi > 45)$, and (f) the number of magnetic null points. The number of magnetic null points and $\dot{H}$ are calculated within the 3D volume; therefore, we cannot study their evolution at different atmospheric heights like the other parameters.

Z. Sun et al. (2024) observed that flare-productive active regions consistently accumulate a significant amount of helicity and energy during their emergence phase. Here, we also studied the evolution of $\dot{H}$ in the case of the studied active regions.

During the analysis, not all AR cases showed the parameter above the threshold level. For example, in AR 13664 (see Figure 3(c)), AR 11429, and AR 11520, $\dot{H}$ was above the threshold level two or even more days before the flare. However, in the cases of AR 12158, AR 12673, AR 11692, and AR 12371, $\dot{H}$ was below the threshold, but only slightly: the values of $\dot{H}$ were around 6×10^{39}–7×10^{39}Mx^2 hr^{-1}.

4.8. *Separation Parameter*—S_{l-f}

Large flares are associated with magnetically complex active regions, in particular those classified as $\beta-\gamma$ or $\beta-\gamma-\delta$ in the magnetic classification system (I. Sammis et al. 2000; M. K. Georgoulis et al. 2019; S. Toriumi & H. Wang 2019). The $\gamma-\delta$ classification indicates that the magnetic polarities are irregularly distributed, with no clearly defined bipolar structure, while the δ classification signifies that opposite magnetic polarities coexist within a single umbra or are very closely packed within a penumbra (S. Toriumi & H. Wang 2019). This characterization of an active region is made through visual observation. However, the spatial separation of opposite polarity subgroups within an AR can be characterized using a specific parameter, e.g., the separation parameter S_{l-f}, which was introduced by M. B. Korsós & R. Erdélyi (2016). This parameter provides a quantitative measure of the area-weighted distance between opposite magnetic polarities in an active region. Smaller values of this parameter (<4) indicate closer proximity of opposite polarities, reflecting increasingly complex magnetic configurations that are most prone to producing intense flares.

In the case of AR 13664 (see Figure 2(d)), the active region exhibited significant evolution due to the large amount of flux emerging until May 6th, during which the S_{l-f} parameter showed a strong increasing trend. From May 6th onward, the S_{l-f} parameter began to decrease, indicating that the active region was becoming increasingly complex. The complexity parameter showed a significant decreasing trend prior to the first X-class flare as we moved higher in the lower solar atmosphere. For example, the S_{l-f} parameter fell below 4 about two days before the X1.0 flare with the accompanying fast CME, while at approximately 7 Mm, this occurred 8 hr before the flare.

Focusing on the other studied active regions, we can conclude that the S_{l-f} parameter was below 4 for two or more days prior to the X-class flare and CME pair from the photosphere up to the lower mid-chromosphere for AR 11149 up to ∼5.5 Mm, AR 11520 up to ∼3 Mm, AR 12158 up to ∼2 Mm, and AR 12673 up to ∼1.5 Mm. In the cases of AR 11149, 11520, and 12158, the S_{l-f} parameter was consistently below 4 for nearly the same amount of time at each height because they were in the fully developed phase, while in the case of AR 12673, the S_{l-f} parameter was below 4 at the photosphere for three days. This parameter dropped to below 4 just a day earlier at 1.5 Mm because this active region was also in a developing phase, similar to AR 13664.

For AR 11692 and 12371, which produced M-class flares with fast CMEs, the S_{l-f} parameters vary from 4 to 9. In the case of AR 12371, this variation occurred more than three days before the solar eruptions from the photosphere up to ∼7 Mm. A similar situation was observed for AR 11692, but we could measure the S_{l-f} parameter from the photosphere up to ∼3 Mm, where the value varies between 4 and 9.

4.9. *Percentage of the Total Area Where the Shear Angle Is Greater than 45°*—$\mathcal{A}(\Psi > 45)$

This parameter is the percentage of the total area where the shear angle is greater than 45°, $\mathcal{A}(\Psi > 45)$. The percentage of that parameter provides a quantitative measure of how much of

Table 2
Classification of the 10 Parameters Used in This Study, Based on Their Dependence on Magnetic Field Strength and Their Preferred Atmospheric Height Ranges for Assessing Pre-eruptive Conditions

Category	Parameter	Height Range Where Threshold Is Satisfied	Height Range Where Gradient Is Higher
Magnetic field strength dependent	Total unsigned magnetic flux Φ_{TOT} ($>10^{22}$ Mx)	photosphere—∼7 Mm	photosphere—∼1 Mm
⋯	Horizontal magnetic gradient G_S ($>10^5$ G pixel^{-1})	photosphere—∼4 Mm	photosphere—∼1 Mm
⋯	Gradient-weighted neutral line length WL_{SG} ($>10^4$ G)	photosphere—∼7 Mm	photosphere—∼1.5 Mm
⋯	Total excess magnetic energy E_e ($> 10^{24}$ erg cm^{-3})	photosphere—∼2 Mm	photosphere—∼0.8 Mm
⋯	Main polarity inversion line length MPIL (>62 Mm)	photosphere—∼7 Mm	photosphere—∼1.5 Mm
⋯	R-value (log (R)> 5)	photosphere—∼0.5 Mm	photosphere—∼0.7 Mm
⋯	Magnetic helicity injection rate $\dot{H}$ ($>4.5 \times 10^{40}$–48×10^{40} Mx^2 hr^{-1})	n/a (calculated over a volume)	n/a (calculated over a volume)
Structural	Separation parameter S_{l-f} (>4)	photosphere—∼7 Mm	n/a (note: evolution changes around ∼4 Mm)
⋯	Shear angle area fraction A(Ψ> 45°)	photosphere—∼7 Mm	photosphere—∼0.8 Mm
⋯	Number of magnetic null points (within 2–10 Mm)	n/a (calculated over a volume)	n/a (calculated over a volume)

Note. Threshold values for each parameter are indicated in brackets next to the parameter name, where applicable.

the region is under high magnetic tension, and consequently, its potential for increased activity or volatility (e.g., M. J. Hagyard et al. 1984; K. D. Leka & G. Barnes 2007).

In our active region sample, we observed that the $\mathcal{A}(\Psi > 45)$ values were approximately 10% higher at the photosphere compared to at 0.36 Mm. Higher than 0.36 Mm, the percentage of $\mathcal{A}(\Psi > 45)$ decreases gradually up to the lower corona. This decrease in percentage is less than 15% up to 7 Mm. The evolution of $\mathcal{A}(\Psi > 45)$ follows a similar pattern at every investigated height before the solar eruptions.

More specifically, in the case of AR 13664 (see Figure 3(e)), four days before the first flares, $\mathcal{A}(\Psi > 45)$ increased from 60% to 70% at the photosphere. About a day before the first flare, it decreased to approximately 55% at the photosphere, while from 0.36 Mm up to the lower corona, the increasing phase is about 15% and the decreasing phase sees a drop of about 20%.

The percentage remained stable for about two days in the cases of AR 11429 at 55% at the photosphere and 35% up to 7 Mm, AR 11520 at 50% at the photosphere and 40% at 7 Mm, AR 11692 at 70% at the photosphere down to 45% at 7 Mm, and AR 12673 at 60% at the photosphere down to 40% at 7 Mm. For AR 12158, the percentage decreased by about 10% at the photosphere from 60% to 55%, and from 0.36 Mm up to 7 Mm, the drop was approximately 15%. In the case of AR 12371, the parameter increased over three days, and about 10 hr before the flare, it dropped by 20% between 0.36 Mm and 7 Mm, from 45% to 30%, with only a 5% drop at the photosphere.

4.10. The Number of Magnetic Null Points

Recent studies have investigated the relationship between magnetic null points and solar flares, with particular focus on the height distribution of these null points in the 2–10 Mm and 10–100 Mm ranges. A notable study by R. L. Edgar & S. Régnier (2024) analyzed several X-class flares during solar cycle 24 and found that the magnetic null points associated with these flares were predominantly located in the lower solar atmosphere, between 2 and 10 Mm, compared to the 10–100 Mm height range.

Regarding our active region analyses, we found that, in general, during the evolution of the active regions, most of the identified null points were located between 2 and 10 Mm prior to the studied eruptions. For instance, in the case of AR 13664, as depicted in Figure 3(f), the number of null points between 2 and 10 Mm (blue curve) aligns closely with the number of null points between 2 and 100 Mm (orange curve), with occasional higher counts between 10 and 100 Mm (green curve), notably about 20 hr before AR 13664's first flare.

However, in the case of AR 12673, approximately half of the null points were within the 2–10 Mm range, with the remainder above 10 Mm. Typically, the number of null points reached its peak a day or even a few days earlier than the largest flares. However, an exception was observed in AR 12158, where the largest flare coincided exactly with the peak number of null points.

4.11. Distinguishing Flux-dependent and Structural Parameters to Trace Height Evolution

Although the parameters were discussed separately above, it is important to note that the 10 parameters could also be grouped into distinct categories—for example, those describing the magnetic complexity of an active region (e.g., S_{l-f} and G_S), those directly related to the properties of the PIL (e.g., the R-value, MPIL, and WL_{SG}), or those linked to magnetic free energy (e.g., E_e and WL_{SG}). However, it is worth emphasizing that these parameters are inherently interconnected, as they all rely on characteristics of the active region that ultimately contribute to solar eruptions. Therefore they all correlate positively with each other and exhibit a degree of redundancy, a known effect that has been demonstrated by previous works (see, e.g., K. D. Leka & G. Barnes 2007; J. A. Guerra et al. 2018; I. Kontogiannis et al. 2018, 2019). Perhaps the most straightforward categorization is to separate them based on whether they explicitly depend on the magnetic field strength. This distinction becomes particularly relevant when studying their evolution at increasing atmospheric heights. Therefore, as summarized in Table 2, we introduce two groups:

1. *Magnetic field value dependent parameters.* Since the magnetic field weakens with height, the values of these (e.g., G_S, R-value, WL_{SG}, MPIL, Φ_{TOT}, and E_e, $\dot{H}$) parameters generally decrease with increasing altitude.
2. *Structural parameters.* These are less sensitive to the magnetic field strength and instead focus on the geometrical or topological properties of the active region. They do not incorporate the field magnitude explicitly. Examples include S_{I-f}, $A(\Psi > 45°)$, and the number of magnetic null points.

Grouping the parameters in this way enables a more targeted interpretation of how their evolution depends on height and may reveal additional underlying eruptive behaviors. Furthermore, Figure 4 presents a summary of the analyses conducted across the studied active regions, ranging from low-energy flares accompanied by major CMEs (e.g., AR 12371 and AR 11692) to powerful X-class flares also associated with significant CMEs (e.g., AR 12673, AR 12158, AR 11520, AR 11429, and AR 13664). The figure shows the number of hours before each solar eruption at which, and within which height range, each parameter met its respective pre-flare threshold condition. When interpreted alongside the categorization in Table 2, the trends in Figure 4 provide a structured framework for understanding pre-eruptive signatures in the solar atmosphere.

In general, the time series evolution of most parameters is similar from the photosphere up to a certain height, with notable exceptions for the number of magnetic null points and the helicity injection rate $\dot{H}$, as these are calculated over a volume rather than a surface. As shown in Figure 2(a), the magnitude of Φ_{TOT} decreases most steeply between the photosphere and 1 Mm. Above 1 Mm, the gradient gradually weakens with increasing height, causing the time series to converge and appear closer to one another. A similar convergence at higher atmospheric layers is observed for other magnetic-field-dependent parameters such as G_S, WL_{SG}, MPIL, and E_e, except for the R-value, which cannot be reliably measured throughout the solar atmosphere and is mostly limited to heights below approximately 0.7 Mm.

Regarding the structural parameters, the magnitude gradient of S_{I-f} remains small; however, a noticeable change in its evolution appears around 4 Mm. This is likely due to the extrapolated magnetic field structure becoming less detailed at greater heights compared to, for example, the photosphere. Similarly, the gradient of $A(\Psi > 45°)$ becomes smaller above approximately 1 Mm, which may be related to the increasing diffuseness of magnetic field elements with height.

Since we examined various flare events, all accompanied by large CMEs, we found that—at this stage—it is most insightful to focus on the maximum height at which each parameter still exceeds its respective threshold level. Based on Figure 4, we conclude that, for most parameters, it is important to extend their application to higher atmospheric layers—in some cases, up to 7 Mm. However, for parameters such as E_e and the R-value, analysis up to approximately 1 Mm appears sufficient. This height-dependent evolution of the parameters serves as an indication of how complex the underlying magnetic field structure remains with altitude. Additionally, grouping the parameters into the two categories described above helps clarify which factors should be considered when interpreting complementary information, ultimately supporting efforts to further improve flare prediction. However, drawing more definitive conclusions will require extending the analysis to a broader data set that includes a wider range of flare and CME intensities, as well as noneruptive (negative) cases.

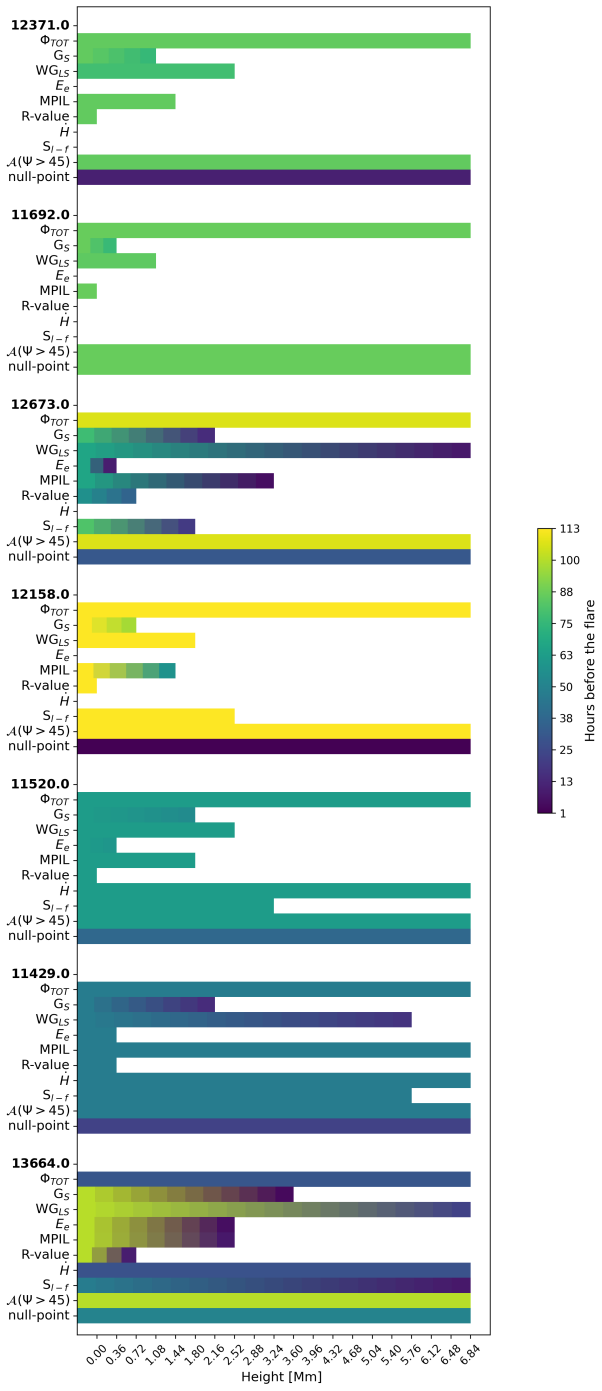

Figure 4. This figure is a summary of the analyses of the studied active regions, showing different parameters as a function of height. The x-axis corresponds to the height in Mm. The y-axis displays the studied active regions and indicates which parameters satisfied their own pre-flare requirements, as discussed in Section 4. The active region name is in boldface, and below each active region name, the notation for the parameters is provided. The full names of the parameters can also be found in the subsections of Section 4. The color bar represents the number of hours before the corresponding solar eruption, indicating how many hours prior to the flare each parameter satisfied its own pre-flare requirements. Note that, if a bar is missing for a given parameter in certain active region cases, it indicates that the parameter did not satisfy the pre-flare condition, as discussed in the relevant subsection of Section 2.

5. Conclusion

Our primary objective in this study is to trace magnetic signatures through the solar atmosphere in seven eruptive active regions. Specifically, we focused on ARs 13664, 11429, 11520, 12158, and 12673, each associated with X-class flares and fast CMEs, while ARs 11692 and 12371 produced M-class flares that were nevertheless accompanied by fast CMEs (see Table 1). These active regions were selected for their relevance to space weather research, as their eruptions triggered geomagnetic storms—making their pre-eruptive evolution particularly valuable for studies investigating the full chain of space weather effects, from the Sun to the Earth.

To analyze the pre-eruptive conditions of these seven active regions, we constructed the 3D magnetic field skeleton of each active region at every time step using the LFFF extrapolation method. We then analyzed the evolution of 10 key parameters throughout the lower solar atmosphere (see Table 2) to characterize the three-dimensional magnetic field structures of each active region. Specifically, we investigated the height ranges in which each parameter satisfied its pre-flare threshold condition prior to the eruption. Based on our analyses, we have come to the following conclusions:

1. Parameters that depend on magnetic field strength—such as $\Phi_{\rm TOT}$, G_S, $\rm WL_{SG}$, E_e, MPIL, and the R-value—show the steepest decrease up to $\sim$1 Mm. Above this, their gradients weaken, leading to convergence in their time series with height. Structural parameters like S_{l-f} and $A(\Psi > 45^\circ)$ vary less with height, though S_{l-f} changes around 4 Mm and $A(\Psi > 45^\circ)$ flattens above 1 Mm, likely due to reduced magnetic detail.
2. When the active region is in the emerging phase, as seen with AR 13664 and AR 12673, the parameters cross the threshold level later, since the magnetic structure is still extending into the solar atmosphere. However, up to 1–1.5 Mm, the threshold level could still be reached by S_{l-f}, MPIL, G_S, and $\rm WL_{SG}$ about a day or even longer before, in the case of X-class events. An exceptional case is AR 13664, which is known to be an anomaly from various aspects (N. M. Kondrashova et al. 2024; I. Kontogiannis 2024; H. Hayakawa et al. 2025). In the case of fully developed active regions, the proxy parameters S_{l-f}, MPIL, G_S, and $\rm WL_{SG}$ only show a few hours difference compared to the photosphere, as they reach the threshold level at the maximum height. In the case of the two M-class flares, the S_{l-f} parameter was above the threshold level, while MPIL, G_S, and $\rm WL_{SG}$ also exceeded their threshold levels at several heights (see Figure 4). Although S_{l-f} alone did not indicate a major eruption, the behavior of MPIL, G_S, and $\rm WL_{SG}$ suggests that AR 12371 and AR 11692 had the potential to produce a large solar eruption.
3. Regarding the percentage of the total area where the shear angle is greater than 45°, the $\mathcal{A}(\Psi > 45)$ parameter gradually decreases up to the lower corona, with a reduction of less than 20% from the photosphere up to 7 Mm. Notably, between the photosphere and 2 Mm, the $\mathcal{A}(\Psi > 45)$ values remained around 40%–50% in the days leading up to the solar eruptions across all active region cases. This indicates that these active regions exhibited significantly high magnetic shear in the lower solar atmosphere, which contributed to the occurrence of large solar eruptions.
4. In most of the active region cases, we found that a large portion—or even all—of the null points were located within the 2–10 Mm range prior to the studied solar eruptions, with the remainder found above 10 Mm. Typically, the number of null points within the 2–10 Mm range peaked a day or even a few days before the largest flares. An exception was observed in AR 12158, where the largest flare coincided exactly with the peak number of null points. In the case of AR 12673, approximately half of the null points were located within the 2–10 Mm range, while the remaining half were found above 10 Mm. The presence of magnetic null points in the lower solar atmosphere is of particular interest, as these locations are favorable sites for magnetic reconnection.
5. The R-value and E_e typically only reach their threshold levels at the photosphere or near its upper boundary, if at all. However, in the case of AR 13664, these parameters satisfied their threshold levels at much higher atmospheric layers, clearly indicating that this active region was a massive giant compared to the others.
6. The $\dot{H}$ exceeded the threshold level in the cases of AR 11520, AR 11429, and AR 13664, which were among the most eruption-productive active regions.

In summary, our results suggest that active regions in which a larger number of proxy parameters exceed their threshold levels at higher atmospheric heights are more likely to produce stronger solar eruptions. This trend is particularly evident in active regions associated with the most energetic events—X-class flares accompanied by fast CMEs—where at least 8 out of the 10 examined parameters reached their threshold levels at higher layers. Conversely, in the cases of AR 11692 and AR 12371, which produced M-class flares with fast CMEs, at least 6 parameters satisfied their thresholds at higher atmospheric heights.

Drawing from these findings on magnetically complex active regions, we recognize significant benefits in broadening the use of diverse prediction parameters within the lower solar atmosphere. Specifically, identifying the atmospheric height range at which predictive parameters meet their pre-eruptive thresholds may significantly enhance the accuracy of forecasting the eruptive potential of active regions. However, to strengthen these conclusions, this analysis will be extended to include both eruptive and noneruptive magnetically complex active regions. Additionally, further exploration is needed to identify which parameters could be effectively utilized if direct chromospheric and coronal magnetic field measurements were available. In the future, we also plan to add more viewpoints and/or higher-resolution data—for example, from Solar Orbiter—to evaluate whether this offers any improvements.

However, we would like to highlight that our results were obtained using LFFF extrapolation, which is computationally efficient but less accurate than NLFFF. This limitation may slightly shift the height intervals at which the parameters exceed their critical thresholds compared to those derived using NLFFF (see M. B. Korsós et al. (2024) for details).

Acknowledgments

The authors are grateful to the referee for providing professional and supportive comments, which helped improve the quality of the manuscript. M.B.K. is grateful to the Leverhulme Trust Fund ECF-2023-271, Science and Technology Facilities Council ST/M000826/1, and to NKFIH OTKA (Hungary, grant No. K142987). F.F. acknowledges support from ASI/INAF agreement No. 2022-29-HH.0 Missione MUSE. F.Z. acknowledges support during the CAESAR project financed by the Italian Space Agency and the National Institute of Astrophysics through the ASI-INAF n.2020-35-HH.0 agreement for the development of the ASPIS prototype of the scientific data center for Space Weather. The ROB team thanks the Belgian Federal Science Policy Office (BELSPO) for the provision of financial support in the framework of the PRODEX Programme of the European Space Agency (ESA) under contract Nos. 4000112292, 4000134088, 4000106864, 4000134474, and 4000136424, SIDC Data Exploitation (ESA Prodex-12).

ORCID iDs

Marianna B. Korsós https://orcid.org/0000-0002-0049-4798
Ioannis Kontogiannis https://orcid.org/0000-0002-3694-4527
Daria Shukhobodskaia https://orcid.org/0000-0001-5302-6253
Luciano Rodriguez https://orcid.org/0000-0002-6097-374X
Fabiana Ferrente https://orcid.org/0000-0002-8070-5048
Francesca Zuccarello https://orcid.org/0000-0003-1853-2550

References

Asai, A., Yokoyama, T., Shimojo, M., et al. 2004, ApJ, 611, 557
Biswal, S., Korsós, M. B., Georgoulis, M. K., et al. 2024, ApJ, 974, 259
Bobra, M. G., Sun, X., Hoeksema, J. T., et al. 2014, SoPh, 289, 3549
Bruzek, A. 1964, ApJ, 140, 746
Buzás, A., Kouba, D., Mielich, J., et al. 2023, FrASS, 10, 1201625
Buzulukova, N., & Tsurutani, B. 2022, FrASS, 9, 429
Chen, P. F. 2011, LRSP, 8, 1
Curto, J. J. 2020, JSWSC, 10, 27
Edgar, R. L., & Régnier, S. 2024, MNRAS, 532, 755
Falconer, D. A., Moore, R. L., Barghouty, A. F., & Khazanov, I. 2012, ApJ, 757, 32
Falconer, D. A., Moore, R. L., & Gary, G. A. 2003, JGRA, 108, 1380
Fletcher, L., Dennis, B.R., Hudson, H.S., et al. 2011, SSRv, 159, 19
Garland, S. H., Yurchyshyn, V. B., Loper, R. D., Akers, B. F., & Emmons, D. J. 2024, FrASS, 11, 1369749
Georgoulis, M. K., Nindos, A., & Zhang, H. 2019, RSPTA, 377, 20180094
Georgoulis, M. K., Bloomfield, D. S., Piana, M., et al. 2021, JSWSC, 11, 39
Georgoulis, M. K., Yardley, S., Guerra, J., et al. 2024, 45th COSPAR Scientific Assembly, Prediction of Solar Energetic Events Impacting Space Weather Conditions: A Roadmap of Findings and Recommendations (Busan: COSPAR), 2903
Gopalswamy, N. 2016, GSL, 3, 8
Guerra, J. A., Park, S. H., Gallagher, P. T., et al. 2018, SoPh, 293, 9
Hagyard, M. J., Smith, J. B., Jr., Teuber, D., & West, E. A. 1984, SoPh, 91, 115
Hayakawa, H., Ebihara, Y., Mishev, A., et al. 2025, ApJ, 979, 49
Hazra, S., Sardar, G., & Chowdhury, P. 2020, A&A, 639, A44
Jarolim, R., Thalmann, J. K., Veronig, A. M., & Podladchikova, T. 2023, NatAs, 7, 1171
Jarolim, R., Veronig, A. M., Purkhart, S., Zhang, P., & Rempel, M. 2024, ApJL, 976, L12
Jaswal, P., Sinha, S., & Nandy, D. 2024, ApJ, 979, 31
Jing, J., Park, S.-H., Liu, C., et al. 2012, ApJL, 752, L9
Kay, C., & Palmerio, E. 2024, SpWea, 22, e2023SW003796
Kondrashova, N. M., Pasechnik, M. M., Osipov, S. M., & Pishkalo, M. I. 2024, OAP, 37, 112
Kontogiannis, I. 2023, AdSpR, 71, 2017
Kontogiannis, I. 2024, A&A, 690, L10
Kontogiannis, I., & Georgoulis, M. K. 2024, ApJ, 970, 162
Kontogiannis, I., Georgoulis, M. K., Guerra, J. A., Park, S.-H., & Bloomfield, D. S. 2019, SoPh, 294, 130
Kontogiannis, I., Georgoulis, M. K., Park, S.-H., & Guerra, J. A. 2018, SoPh, 293, 96
Korsós, M. B., Chatterjee, P., & Erdélyi, R. 2018, ApJ, 857, 103
Korsós, M. B., & Erdélyi, R. 2016, ApJ, 823, 153
Korsós, M. B., Erdélyi, R., Huang, X., & Morgan, H. 2022, ApJ, 933, 66
Korsós, M. B., Jarolim, R., Erdélyi, R., et al. 2024, ApJ, 962, 171
Korsós, M. B., Georgoulis, M. K., Gyenge, N., et al. 2020, ApJ, 896, 119
LaBonte, B. J., Georgoulis, M. K., & Rust, D. M. 2007, ApJ, 671, 955
Lakhina, G. S., & Tsurutani, B. T. 2016, GSL, 3, 5
Leka, K. D., & Barnes, G. 2003, ApJ, 595, 1277
Leka, K. D., & Barnes, G. 2007, ApJ, 656, 1173
Li, T., Chen, A., Hou, Y., et al. 2021, ApJL, 917, L29
Li, Y., Liu, X., Jing, Z., et al. 2024, ApJL, 972, L1
Lin, P. H., Kusano, K., Shiota, D., et al. 2020, ApJ, 894, 20
Liokati, E., Nindos, A., & Liu, Y. 2022, A&A, 662, A6
Lu, Y., Wang, J., & Wang, H. 1993, SoPh, 148, 119
MacTaggart, D., Williams, T., & Aslam, O. 2024, JGRA, 130, e2024JA033462
Mason, J. P., & Hoeksema, J. T. 2010, ApJ, 723, 634
Miteva, R., Nedal, M., Veronig, A., & Pötzi, W. 2024, Atmos, 15, 930
Moon, Y. J., Chae, J., Choe, G. S., et al. 2002, ApJ, 574, 1066
Pagano, P., Mackay, D. H., & Yardley, S. L. 2019, ApJ, 886, 81
Park, S.-h., Chae, J., & Wang, H. 2010, ApJ, 718, 43
Patari, A., & Guha, A. 2023, AdSpR, 71, 5147
Pesnell, W. D., Thompson, B. J., & Chamberlin, P. C. 2012, SoPh, 275, 3
Romano, P., Elmhamdi, A., Marassi, A., & Contarino, L. 2024, ApJL, 973, L31
Sammis, I., Tang, F., & Zirin, H. 2000, ApJ, 540, 583
Scherrer, P. H., Schou, J., Bush, R. I., et al. 2012, SoPh, 275, 207
Schrijver, C. J. 2007, ApJL, 655, L117
Shanmugaraju, A., Vijayalakshmi, P., Lawrance, M. B., Moon, Y.-J., & Ebenezer, E. 2023, JASTP, 249, 106106
Shibata, K., & Magara, T. 2011, LRSP, 8, 6
Sun, Z., Li, T., Wang, Q., et al. 2024, A&A, 686, A148
Thernisien, A. 2011, ApJS, 194, 33
Thernisien, A., Vourlidas, A., & Howard, R. A. 2009, SoPh, 256, 111
Toriumi, S., & Wang, H. 2019, LRSP, 16, 3
Verbeke, C., Mays, M. L., Kay, C., et al. 2023, AdSpR, 72, 5243
Wang, J., Shi, Z., Wang, H., & Lue, Y. 1996, ApJ, 456, 861
Wang, R., Liu, Y. D., Zhao, X., & Hu, H. 2024, A&A, 692, A112
Webb, D. F., & Howard, T. A. 2012, LRSP, 9, 3
Wiegelmann, T., & Sakurai, T. 2021, LRSP, 18, 1
Wiegelmann, T., Thalmann, J. K., Inhester, B., et al. 2012, SoPh, 281, 37